PLANETARY SCIENCE

Changing spatial distribution of water flow charts major change in Mars's greenhouse effect

Edwin S. Kite[1]*, Michael A. Mischna[2], Bowen Fan[1], Alexander M. Morgan[3,4], Sharon A. Wilson[3], Mark I. Richardson[5]

Early Mars had rivers, but the cause of Mars's wet-to-dry transition remains unknown. Past climate on Mars can be probed using the spatial distribution of climate-sensitive landforms. We analyzed global databases of water-worked landforms and identified changes in the spatial distribution of rivers over time. These changes are simply explained by comparison to a simplified meltwater model driven by an ensemble of global climate model simulations, as the result of ≳10 K global cooling, from global average surface temperature $\overline{T} \geq 268$ K to $\overline{T} \sim 258$ K, due to a weaker greenhouse effect. In other words, river-forming climates on early Mars were warm and wet first, and cold and wet later. Unexpectedly, analysis of the greenhouse effect within our ensemble of global climate model simulations suggests that this shift was primarily driven by waning non-CO_2 radiative forcing, and not changes in CO_2 radiative forcing.

INTRODUCTION

Mars's climate 3.6 to 3.0 billion years (Ga) ago was at least occasionally warm enough for rivers and lakes (inferred to have been habitable) [e.g., (*1*–*4*)), but the surface today is a cold desert. Few constraints exist on Mars's atmospheric greenhouse effect during the wet-to-dry transition (*4*). Was early Mars temperate or icy, was the environmental catastrophe abrupt or gradual, and what caused the change? The prevailing view is that the cause of Mars's drying-out was loss of atmospheric CO_2. Mars's atmosphere today is so thin (~6 mbar, CO_2-dominated) that it is close to the triple point of water, so lakes on early Mars probably formed under a thicker atmosphere (*5*–*7*). CO_2 is, in the modern inner solar system, a key greenhouse gas for regulating climate change (*8*). However, even when H_2O vapor feedback is considered, additional non-CO_2 warming is needed to warm early Mars enough for rivers (*9*). Therefore, changes in non-CO_2 radiative forcing are an alternative explanation for Mars's wet-to-dry transition. The relative importance of these two mechanisms has not been investigated, so the prevailing explanation of the wet-to-dry transition remains untested.

Here, we reconstruct the history of Mars's greenhouse effect using geologic proxies for past river activity that time-resolve Mars's desertification. We compare the proxy data to a climate model to retrieve changes in the greenhouse effect and also to assess the extent to which the changes were the result of changes in CO_2 radiative forcing versus non-CO_2 radiative forcing. Last, we discuss the implications for the cause of the cooling and drying-out of Mars.

Our approach uses Mars's geologic record of precipitation-fed water runoff (meltwater and/or rain) spanning multiple eras [e.g., (*3*–*4*) and references therein] (fig. S2). Early on (>3.6 Ga ago), spatially pervasive and regionally integrated valley networks formed (*10*). Later, 3.6 to 3.0 Ga ago (and perhaps still later), spatially patchy alluvial fans (and some deltas) formed [e.g., (*2*–*3*)]. The fans mostly did not result from localized impact-induced precipitation and record a time span of >20 million years of river flow (*2*,*11*). Data suggest that during this period, conditions were only intermittently wet enough for surface runoff [e.g., (*4*, *12*–*15*)]. The early period of valley networks and the later formation of alluvial fans show distinct spatial distributions of rivers (Fig. 1). (We exclude rivers not formed by precipitation, e.g., associated with groundwater outbursts, as well as other features that might record nonprecipitation processes; see the Supplementary Materials.) We use the shifts in the spatial distribution of precipitation-fed rivers (Fig. 1) to assess past changes in the strength of the atmospheric greenhouse effect. In broad outline, this approach has been attempted previously, using Viking data to analyze pre–valley network era changes (*16*). Here, we study post–valley network era change using new data and new models, and draw a different conclusion.

RESULTS

Charting the decline of Mars's surface habitability

Given its potential as a probe of the ancient greenhouse effect, it is perhaps unexpected that Mars's paleo-river distribution has not previously been analyzed for latitude/elevation trends with correction for detectability biases. We analyze river-distribution databases for >3.6-Ga valley networks (*17*) and for <3.6-Ga rivers (see the Supplementary Materials) (*18*). Both databases are corrected for postfluvial resurfacing (i.e., detectability/preservation bias), masking out the areas shown in dark gray in Fig. 1 (the basis for this masking is explained in the Supplementary Materials).

To plot the elevations of <3.6-Ga rivers, we used the mean of the Mars Orbiter Laser Altimeter (MOLA) elevation of each of the eroded topographic catchments draining into observed fans and deltas. To plot the elevations of >3.6-Ga rivers, we used the topographic elevation of points midway along each (erosional) valley segment. Therefore, the comparison of the elevations of eroded pre–3.6-Ga landforms to the elevations of eroded post–3.6-Ga landforms is an apples-to-apples comparison (Fig. 2).

Contrary to uncorrected catalogs, valley networks formed preferentially at higher elevations than later-stage fluvial features (Fig. 2). At high elevations during the valley network era, there must have been a source of water (snow, ice, or rain), and to produce runoff,

[1]University of Chicago, Chicago, IL 60637, USA. [2]Jet Propulsion Laboratory, California Institute of Technology, Pasadena, CA 91109, USA. [3]Smithsonian Institution, Washington, DC 20002, USA. [4]Planetary Science Institute, Tucson, AZ 85719, USA. [5]Aeolis Research, Chandler, AZ 85224, USA.
*Corresponding author. Email: kite@uchicago.edu

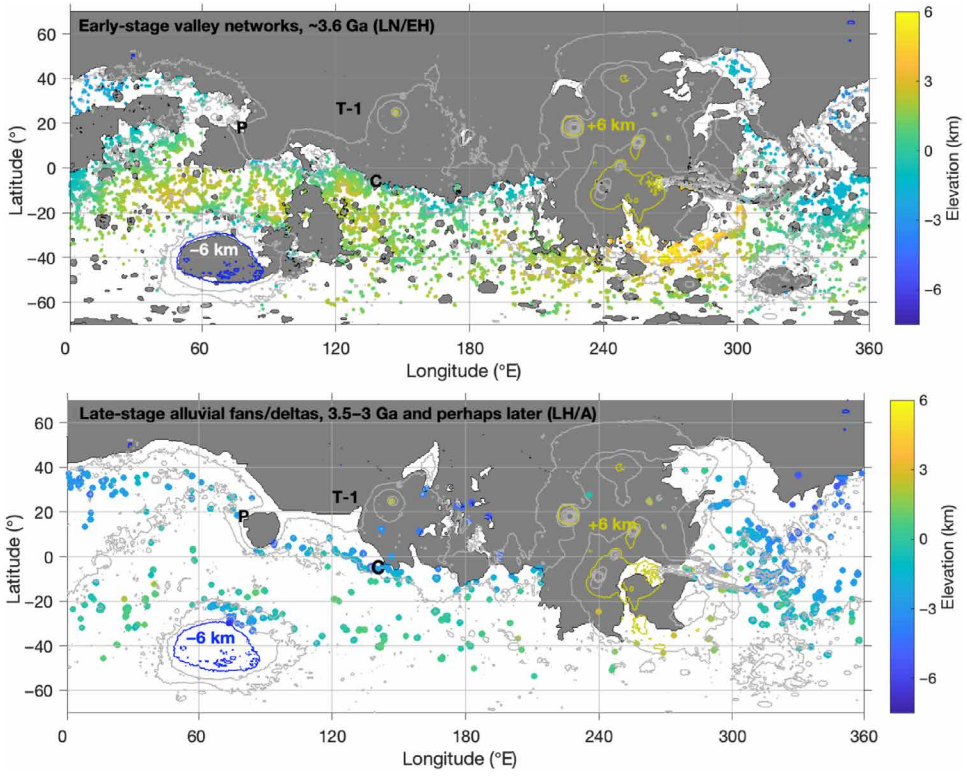

Fig. 1. Changing spatial distribution of water flow on Mars. (**Top**) Distribution of >3.6-Ga [Late Noachian/Early Hesperian (LN/EH)] rivers (*17*). Color: River elevation. Gray: Excluded region (low/no detection probability). Rivers plotting within gray region are shown by black dots. Rovers: C, Curiosity at Gale crater; P, Perseverance at Jezero crater; T-1, Tianwen-1 rover (Zhurong). Elevation contour spacing is 3 km. (**Bottom**) Distribution of <3.6-Ga [Late Hesperian/Amazonian (LH/A)] rivers (*18*).

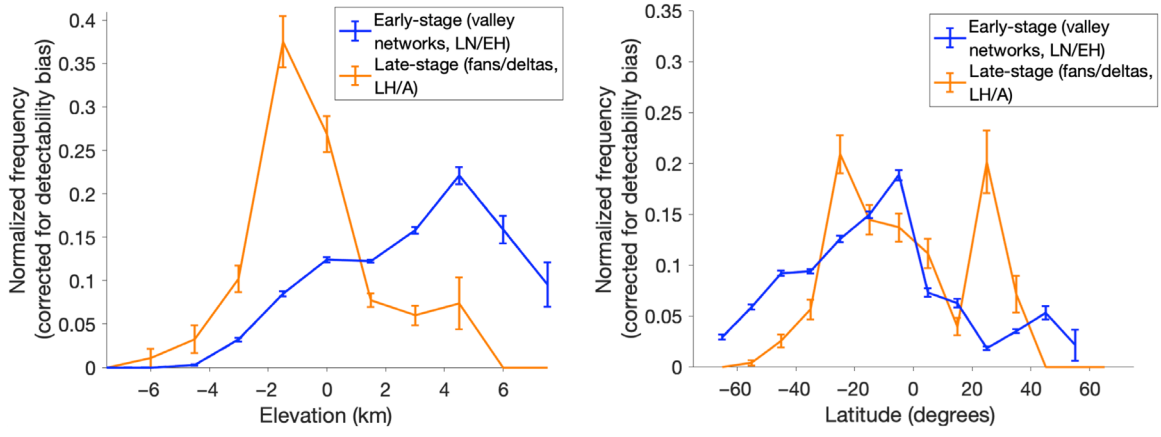

Fig. 2. Decline over time in elevation of water-worked landforms, corresponding to a shift from >3.6-Ga elevation control to <3.6-Ga latitudinal banding. Normalized frequencies (±1σ) of the elevation (**left**) and latitude (**right**) distribution of fluvial features on early Mars (valley networks) and later Mars (fans/deltas). Figures S3 to S5 give more details and sensitivity tests.

the surface temperature, T_{surf}, must have exceeded 273 K, at least intermittently [e.g., (*9*, *19*)]. A very strong atmospheric greenhouse effect is required during the early (valley network, >3.6 Ga) era.

We neglect postfluvial true polar wander (TPW) because it was likely minor (see the Supplementary Materials). Indirect geologic proxies have been used to infer post–valley network TPW (*20*), but these are affected by resurfacing biases. If post–valley network TPW was ~20°, then the finding that valley networks formed at high elevation (Fig. 2) would be unaffected. Wiggling of the southern midlatitude band of <3.6-Ga rivers is well explained by coupling between atmospheric water transport and topography, without TPW (*21*).

Global climate model

Surface liquid water requires a supply of H_2O (e.g., snow or rain) and temperatures above freezing. Temperature would not be limiting if Mars had a very strong greenhouse effect, and surface liquid

water would occur, at least seasonally, wherever H_2O was available. If (as on Earth) the coldest parts of the surface act as a cold trap for snow and ice, then H_2O would be available at locations where snow/ice is most stable, on a planetary surface that had only (3 ± 2)% of Earth's area-averaged H_2O abundance (*22*). By contrast, on a planet with a greenhouse effect that was weaker (but still stronger than on modern Mars), temperature would be limiting and liquid water could occur only in relatively warm locations.

To explore how changing patterns of surface temperature (T_{surf}) and snow/ice stability are driven by changes in P_{CO_2} (partial pressure of CO_2), non-CO_2 radiative forcing, and orbital forcing, we used the Mars Weather Research and Forecasting Model (MarsWRF) global climate model (GCM) (see Materials and Methods) (*23*–*24*). CO_2 greenhouse warming is insufficient to explain pre–3.0-Ga rivers on Mars (*7*). Similar to (*25*–*26*), our model represents the unknown, non-CO_2 greenhouse-warming agent by a gas with wavelength-independent "gray" opacity (κ) in the thermal infrared, with no opacity at solar wavelengths, and which does not contribute to total pressure. In previous modeling work investigating leading candidate agents of non-CO_2 greenhouse warming, these agents contribute little to total pressure [probably <20%; (*19*)] and are fairly well mixed horizontally; therefore, this representation is reasonable. CO_2 and the gray gas are the only species in the model. Solar luminosity is set to 80% of the modern value (*27*). Surface albedo and thermal inertia are set to uniform values of 0.2 and 250 J m^{-2} K^{-1} $s^{-½}$, respectively, which are close to Mars's average bare-ground values. The model is run to equilibrium, and all output subsequently discussed is from the analysis of final-year output.

Our approach is to simply represent key physical processes in a fast-running model with relatively few adjustable parameters, including three-dimensional (3D) topography as is necessary for comparison to paleo-river spatial distributions. This approach sits between that of 1D/2D models and fully coupled GCMs. The most important limitation of our approach is that we do not simulate rainfall, although (as described below) we do test for the internal consistency and plausibility of meltwater runoff.

First, using CO_2-only runs, we reverified (*9*) that at 1000-mbar P_{CO_2}, snow is most stable on high ground, and the temperature dependence on latitude is, while still substantial, relatively modest. Still higher atmospheric pressures would produce the same pattern (*9*, *19*). A 20-mbar P_{CO_2} CO_2-only simulation is much colder, with strong latitudinal banding in T_{surf} and snow stability. This is consistent with <1.5-Ga geologic data [e.g., (*28*)].

Next, we switched gray gas forcing on. For the strong non-CO_2 radiative forcing that is needed to explain geologic data, the surface temperature lapse rate (i.e., $\partial T_{surf}/\partial z_{topo}$, where z_{topo} is the topographic elevation relative to the geoid) is approximately the atmospheric adiabatic lapse rate for all surface pressures. Greenhouse forcing, and not the density-dependent turbulent fluxes between the atmosphere and the ground, regulates the surface temperature lapse rate. Therefore, paleo-proxies for the atmospheric adiabatic lapse rate cannot be used as a paleo-barometer for steady-state wet climates on early Mars.

Last, we ran 54 GCM simulations defining a 3 × 9 × 2 parameter space (table S1), varying P_{CO_2} (20, 150, and 500 mbar), non-CO_2 radiative forcing [9 values log-evenly spaced from τ = 1.7 to τ = 4.5, where $\tau = \kappa \times (P_{CO_2}/3.7\ m\ s^{-2})$], and orbital forcing (25° and 45° obliquity; obliquity is the most important orbital parameter for controlling Mars's climate). These parameters span a very wide range of greenhouse conditions, from globally subfreezing up to warming strong enough for runoff everywhere on the planet. These parameters span the range of plausible parameters for early Mars river-forming climates.

Using the surface temperature and near-surface wind field output from the model, we calculated the likelihood of seasonal meltwater. First, we downscaled the 64 × 48 grid point GCM output to ~7 km per pixel using MOLA gridded topography. Temperature was downscaled using the run-by-run correlation between mean temperature and elevation for latitudes <30°, and pressure was downscaled assuming a fixed scale height of 10.7 km. Following (*25*) and (*29*), we assume that snow tends to accumulate in locations that minimize the annually integrated sublimation rate. For example, on Earth, high ground acts as a cold trap for snow and ice (*9*). (Mars's topography has a range and SD 3.5× greater than Earth's.) If so, cold traps contain snow and ice that (if temperatures get warm enough) becomes a water source for runoff during melt events (*9*). We represent this effect by a postprocessing parameter, f_{snow}, corresponding to the areal fraction of the planet that has snow during the warm season. For a given value of f_{snow}, we check if any pixels with sublimation rates less than the threshold defining f_{snow} have warm-season temperatures (mean temperatures for a continuous period of 100 sols) >273 K. The 100-sol requirement is to allow time for thermal maturation of snow/ice for runoff production (*30*). [This is conservative, and in the Antarctic dry valleys, lake levels respond more quickly to temperatures above freezing; (*31*, *32*)]. Such pixels are designated as runoff pixels. We refer to this procedure as the simplified meltwater model. Evaporitic cooling is not considered. For each GCM run, we repeat this for $f_{snow} = \{0.01, 0.02 \ldots 1\}$ to generate possible meltwater maps.

Comparing model output to geologic data

We compare each map to the two geologic time slices (Fig. 1), assigning every (~7 × 7 km) pixel as a true positive (runoff predicted, ≥1 water-worn features observed), true negative (no runoff predicted or water-worn featured observed), false positive (FP; runoff predicted, but no water-worn feature observed), or false negative (FN; no runoff predicted, but ≥1 water-worn features observed). We cosine-weight to correct for latitude. We marginalize over f_{snow} by calculating (for each of the 54 GCM simulations) (i) a receiver-operating characteristic (ROC) curve varying f_{snow} and measuring the area under the curve (AUC), (ii) informedness (Youden's J statistic, defined as sensitivity + specificity − 1; see the Supplementary Materials), and (iii) the precision-recall AUC (PR-AUC). These calculations treat all values of f_{snow} as equally likely, which represents our uncertainty about the early Mars hydrologic cycle. Our procedure penalizes FPs and FNs equally (see the Supplementary Materials). The three measures agree on which GCM run is the best fit for ~3.6 Ga, and the three measures agree on which GCM run is the best fit for <3.6 Ga.

For the valley network era (>3.6 Ga), Global annual average temperature, $\overline{T}$, is 268 K [Fig. 3 (top)]. The model with the highest informedness (largest value of Youden's J statistic) [ROC AUC 0.68; Fig. 4 (top)] corresponds to $\tau = 3.1$ ($\kappa = 5.7 \times 10^{-4}$), high (45°) obliquity, $f_{snow} = 0.43$, and P_{CO_2} = 150 mbar. Seasonal meltwater runoff occurs over ~40% of the planet. Highland valley networks sit within the meltwater runoff zone. Meltwater runoff is absent at high latitudes and low elevations because warm-season snow is not stable there. [At 45° obliquity, high-latitude snow is destabilized by hot summer

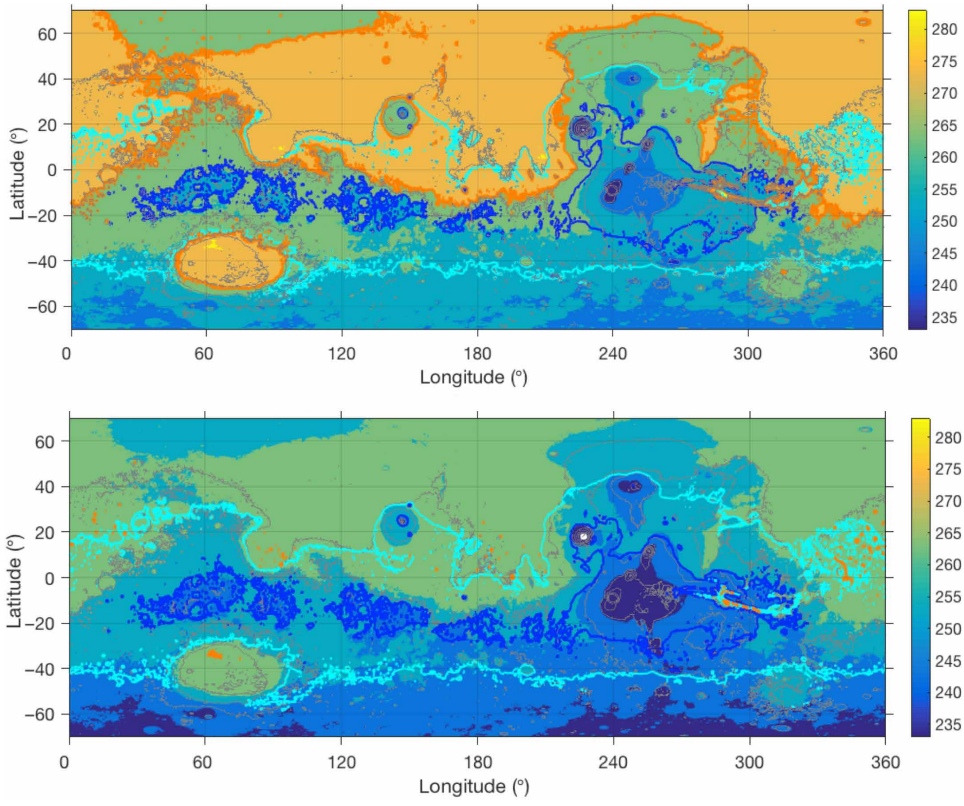

Fig. 3. Global climate model output. (**Top**) Annual average output for GCM run that best matches ~3.6-Ga data ($\tau = 3.14$, 45° obliquity, $P_{CO_2} = 150$ mbar). Color shading corresponds to annual average temperature (K). Orange line highlights 273-K isotherm, and color bands mark 10-K intervals. Dark blue and cyan contours outline cold traps. The dark blue contours contain the part of the planet's surface area with the lowest annually integrated snow sublimation rate (0 to 10th percentile), and the cyan contours contain the part of the planet's surface area with lower-than-average annually integrated snow sublimation rate (0 to 50th percentile). Output (64 × 48) is downscaled using MOLA topography. Elevation contours (gray) are spaced at 3-km intervals. (**Bottom**) As (A), but for the GCM run that best matches 3.5-Ga to 3.0-Ga data ($\tau = 2.46$, 45° obliquity, $P_{CO_2} = 150$ mbar).

solstices; (*33*).] Still-warmer climates [e.g., (*34*)]—but not colder climates—also give good fits to the valley network data. (Global annual average temperature $\overline{T} \geq 273$ K is required to explain all valley networks with a single forward model, at the cost of a slightly increased proportion of FPs.) In the best-fit model, annual average temperatures above freezing exist over much of the northern lowlands and in low spots including Gale crater and Jezero crater [Figs. 3 (top) and 4 (top)]. Many valley networks drain into these broad, no-permafrost zones.

For the fans era (<3.6 Ga), the highest informedness model [ROC AUC 0.65; Fig. 4 (bottom)] corresponds to $\tau = 2.5$ ($\kappa = 4.4 \times 10^{-4}$), 45° obliquity, $f_{snow} = 0.55$, and $P_{CO_2} = 150$ mbar. This shows a much colder ($\overline{T} \sim 258$ K) planet. The highest ground is too cold for meltwater runoff [Fig. 3 (bottom)], the low elevations (and high latitudes) are too warm for snow, and so meltwater runoff occurs at intermediate elevations, consistent with data. Notably, comparing the best-fit <3.6-Ga model to the best-fit 3.6-Ga model (Fig. 3), the changing spatial distribution of water flow on Mars does not require any change in P_{CO_2}. All current rover landing sites, plus the Rosalind Franklin landing site, are predicted to have meltwater runoff production <3.6 Ga. Permafrost temperatures occur almost everywhere, and so shallow-subsurface ice might protect surface water from loss to infiltration (at least temporarily). Infrequent spots with annual average temperatures above freezing, which would have unfrozen and therefore permeable subsurfaces, correspond to areas of known or suspected salt accumulation. This prediction is consistent with the groundwater-upwelling model for sulfate-deposit genesis (*35*). Geographically, the model performs well except for FNs in north Arabia. Given the simplifications of our model, we cannot completely rule out an alternative option for the fans-forming climate that is warm and dry, but it is not favored by our model. A decisive future test is to use the Curiosity rover to search for meridianiite ($MgSO_4 \bullet 11H_2O$), which is unstable above 275 K.

How does the goodness of fit of the model to the data vary as a function of parameter values? Within the model, for both time slices, high obliquity is always favored over low obliquity. [By contrast, rainfall models permit low-obliquity river-forming climates; e.g., (*36*).] This is because, at low obliquity, the low latitudes (and especially high elevations at low latitude) are not particularly favored for meltwater runoff because snow is relatively unstable there, but that is where the valleys are. It remains possible that the patterns in Figs. 1 and 2 are a palimpsest built up over a wide range of orbital forcings that cannot be represented by a run at a single obliquity value. This palimpsest hypothesis is one possible explanation for the valley networks in the southernmost highlands. Whether or not this hypothesis is true, high obliquity during the wet era is still favored. As high (45°) obliquities are favored for both time slices, changes in orbital forcing do not explain the changes between the two periods.

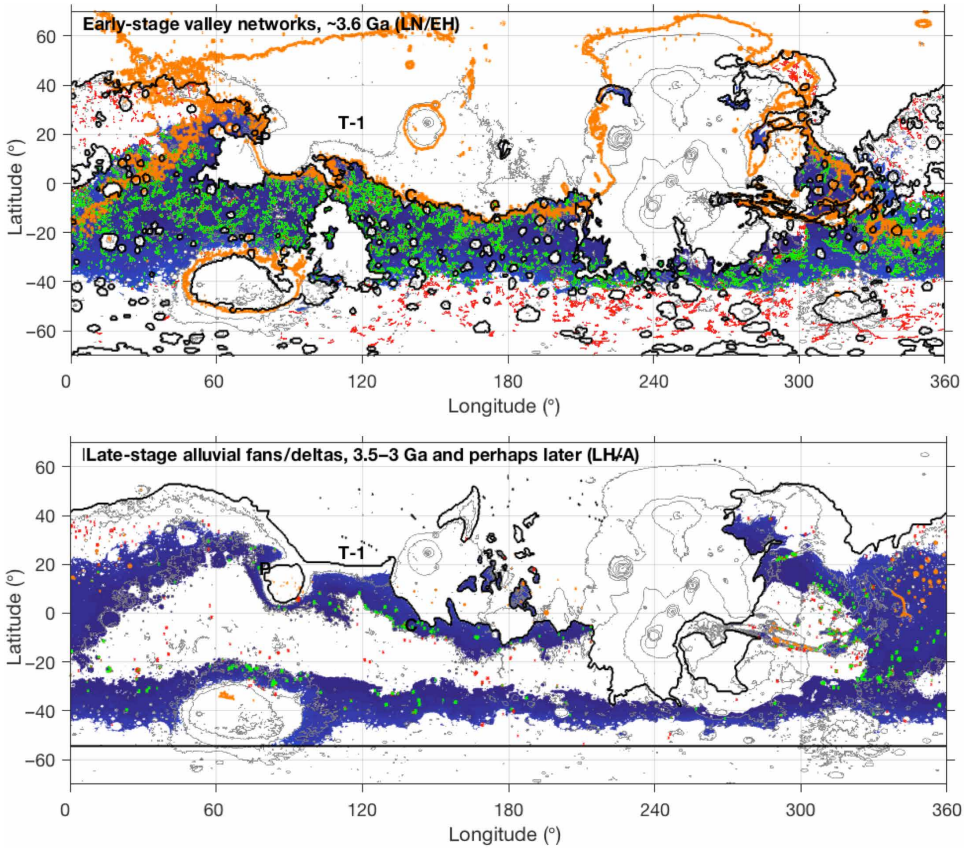

Fig. 4. Comparison of data to model predictions. (**Top**) Data-model comparison for simplified snowmelt model output that best matches ~3.6-Ga data ($\tau = 3.1$, 45° obliquity, $P_{CO_2} = 150$ mbar, $f_{snow} = 43\%$). Dark blue band corresponds to area of snowpack with a continuous 100-sol period with average temperature exceeding 273 K, corresponding to predicted snowmelt runoff. Green symbols correspond to true positives (mapped water-worn features within the predicted snowmelt runoff zone). Red symbols correspond to FNs (mapped water-worn features outside the predicted snowmelt runoff zone). The thick black line outlines the masked-out region (low/no detection probability for water-worn features), which differs between the two eras. Uncommon gray symbols show water-worn features within the masked-out area. Elevation contours (gray) are spaced at 3-km intervals. The orange line highlights the 273-K isotherm in annual average temperature (Youden's J, 0.30; ROC AUC for varying f_{snow} for this GCM, 0.68). Rovers: C, Curiosity; P, Perseverance; T-1, Tianwen-1 rover (Zhurong). (**Bottom**) As (A), but for the simplified snowmelt model output that best matches 3.5-Ga to 3.0-Ga data ($\tau = 2.46$, 45° obliquity, $P_{CO_2} = 150$ mbar, $f_{snow} = 56\%$) (Youden's J, 0.34; ROC AUC for varying f_{snow} for this GCM, 0.65).

Figure 5 shows the trade-off between τ, P_{CO_2}, and model goodness. From this figure, we make the following observations.

First, although the contours slope up and to the right, this slope is gentle. Thus, τ matters more than P_{CO_2}. This is unexpected, as regulation of P_{CO_2} is central to our understanding of planetary habitability (*7*, *8*, *37*). This result can be understood in terms of the high value of τ needed to match data. As τ is high in all infrared bands, the additional contribution to warming from the direct radiative effect of CO_2 is small and counteracted by the increase in planetary albedo due to Rayleigh scattering. Of the runs warm enough to generate rivers, 150-mbar output has similar annual average temperature to the 500-mbar output. Therefore, decline in direct radiative forcing from CO_2 corresponding to P_{CO_2} decline from ~0.5 to ~0.15 bar was probably not the cause of the decline of Mars rivers. Within this P_{CO_2} range, where T_{surf} depends only weakly on P_{CO_2}, carbonate-silicate weathering feedback could have only a weak direct effect on climate. However, an indirect effect (through the effect of P_{CO_2} on the strength of H_2-CO_2 collision-induced absorption warming) remains possible. Because non-CO_2 radiative forcing is an increasing function of P_{CO_2} for some proposed non-CO_2 warming mechanisms (*38*), the door is still open to CO_2 decline being the ultimate driver of the decline of Mars rivers. Nevertheless, the focus shifts to the influence of non-CO_2 warming agents as a function of time.

Second, it was previously proposed (*9*) that the valley networks' high-elevation preference indicates $\gg 10^2$ mbar paleo-P_{CO_2}. However, Fig. 5 shows that these data can also be well matched when P_{CO_2} is ~20 mbar.

Third, the best fits for <3.6 Ga are ~10 ± 5 K colder than the best fits for ~3.6 Ga. This makes sense given the downshift of ~5 km in zonally averaged river abundance (Fig. 2), assuming a surface temperature lapse rate of ~2.5 K/km. Zonal variations are not enough to confound this pattern. We infer that the lack of high-elevation <3.6-Ga rivers indicates a weaker total greenhouse effect at these later times so that high-elevation precipitation stayed frozen. The drop in τ was likely bigger than Fig. 5 (right) suggests, as solar brightening occurred during Mars's wet era but is not included in the model.

Fourth, the τ for <3.6 Ga is well constrained [Fig. 5 (right)]. This corresponds to $\overline{T}$ ~ 258 K and a largely frozen Mars. The cold paleotemperatures inferred from the spatial distribution of fans are consistent with other indications of snowmelt runoff, such as patchy erosion,

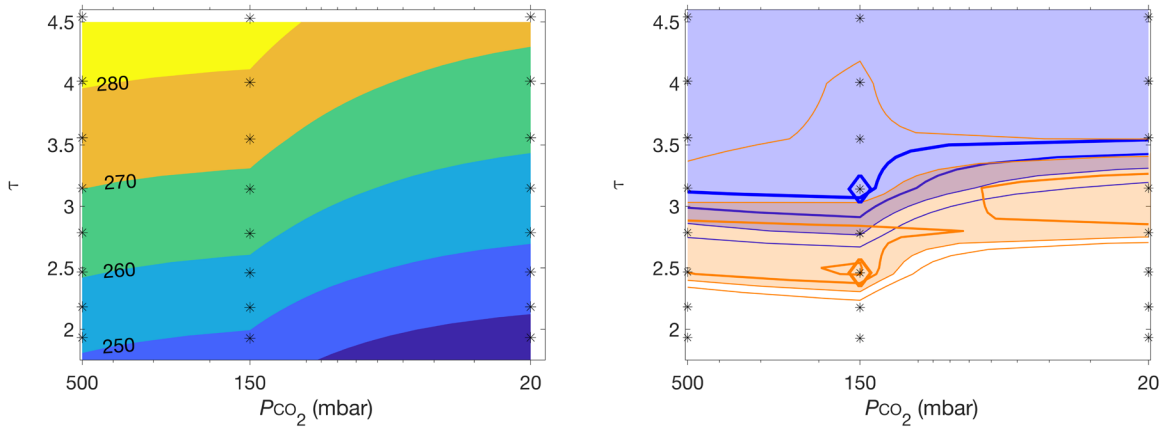

Fig. 5. Best-fit Mars climate versus time. (**Left**) Global annual average temperature (K) as a function of P_{CO_2} and of gray gas column optical depth, τ. Black asterisks correspond to inputs to individual GCMs, and values between the asterisks are interpolated. Obliquity = 45°. (**Right**) Goodness of fit of model to data as a function of P_{CO_2} and of gray gas column optical depth, τ. Blue shaded region corresponds to relatively good fit to >3.6-Ga data, and orange shaded region corresponds to relatively good fit to <3.6-Ga data. The blue diamond is the best-fitting GCM run for >3.6-Ga data, and the orange diamond is the best-fitting GCM run for <3.6-Ga data. Metric is ROC AUC; contours correspond to 0.5, 0.55, 0.6, and 0.65 (thicker lines correspond to better fit). Asterisks correspond to inputs to individual GCMs, and values between the dots are interpolated. Figures S14 and S15 give more details and sensitivity tests.

the absence of channels on fans, and reports of aspect dependence (*18*). It remains to be seen if a rainfall model can match the data equally well.

Last, the best fit for >3.6 Ga is $\overline{T}$ ~ 268 K, and the upper limit is essentially unconstrained. This is consistent with the idea that early Mars had $\overline{T} \geq 280$ K, with rainfall, especially if there were seas at low elevations (*31*, *39*). On the other hand, if temperature was around the best-fit value and low elevations were dry, then most locations would have little or no rainfall.

In summary, we obtained paleo-temperature estimates during the crucial interval when Mars was drying out (3.6 to 3.0 Ga ago and perhaps later). The result is consistent with estimates obtained using other methods. Overall, data-model comparison shows that changes over time in the distribution of Mars paleo-rivers in space (Figs. 1 and 2) are consistent with the expectation that Mars's greenhouse effect waned (perhaps nonmonotonically) over time (Figs. 3 and 4). However, we did not find evidence from this method that the decline of surface habitability on Mars was associated with loss of atmospheric CO_2 (Fig. 5).

DISCUSSION

Our forward model has limitations. Because warm-season temperatures and snow-covered areas are both derived from the same simulated year of GCM output, very rapid shifts in climate (too fast for snow/ice to relocate) cannot be included. This might contribute to the false negatives in northern Arabia Terra. Also, we do not include the albedo effects of snow [in effect, assuming dusty snow; (*29*, *30*, *40*)]. Higher snow albedo would drive our best fits to higher $\overline{T}$ and set a correspondingly more stringent constraint on the strength of non-CO_2 warming needed to match data. It is possible that early Mars's atmosphere spent most of the time in a much colder state than shown in Fig. 5 (e.g., collapsed). In that case, our results still constrain the climate at times when Mars's climate supported rivers and lakes, so this is not a severe limitation.

To what extent are shifts in river distribution explained by the apparent threefold decrease since 3.5 Ga in the inventory of Mars's surface/near-surface H_2O (*41*)? H_2O loss does not fully explain changes in river distribution. For example, groundwater table control does not explain the existence of mid-elevation rivers at 20°S to 40°S (Fig. 1B). A weakening of the greenhouse effect is a simpler explanation for the data. The simplified meltwater model does not constrain the volume of surface/near-surface H_2O (the f_{snow} parameter describes the area of surface H_2O cover, not H_2O volume). The simplified meltwater model provides a simple description of the observed changes, but fully coupled global modeling of both the atmospheric and groundwater parts of the early Mars water cycle has not yet been done. Therefore, determining whether H_2O loss had a large or a small contribution to the observed changes remains a target for future work.

Our analysis suggests that the shifts in river distribution were driven by loss of non-CO_2 radiative forcing. The subsequent [<3 Ga; (*3*, *42*)] cessation of river-forming climates on Mars could have been caused by further reduction in non-CO_2 greenhouse warming (perhaps the simplest explanation), by H_2O loss, or by C loss (Fig. 6). The present-day rate of C escape to space is small (*43*), and isotopic evidence indicates that most of Mars's atmosphere was lost >3.5 Ga ago [e.g., (*44*, *45*)]. Candidate carbon sinks include escape to space, carbonate formation, and basal melting of CO_2 ice. Alternatively, CO_2 could have been reversibly sequestered as CO_2 ice.

Major open questions remain, including the identity of the non-CO_2 greenhouse forcing agent that must have been in the atmosphere (at least intermittently) until ~3 Ga (Fig. 5). Although H_2O vapor feedback would add to warming in all cases, it is insufficient (*9*). Hypotheses for the mechanisms for the needed additional warming include H_2-CO_2 collision-induced absorption [e.g., (*38*, *46*, *47*)] or high-altitude water ice clouds (*48*, *49*). It is possible for either of these two mechanisms to provide very strong (stronger than needed to match data) warming, and this study provides new constraints on how much opacity is needed, and how this requirement changed over geologic time. These hypotheses can be tested using the Perseverance rover. Perseverance observation of detrital siderite (±fine-grained olivine) would favor moderate river pH and thus low P_{CO_2} during the years of river flow, potentially excluding warming by

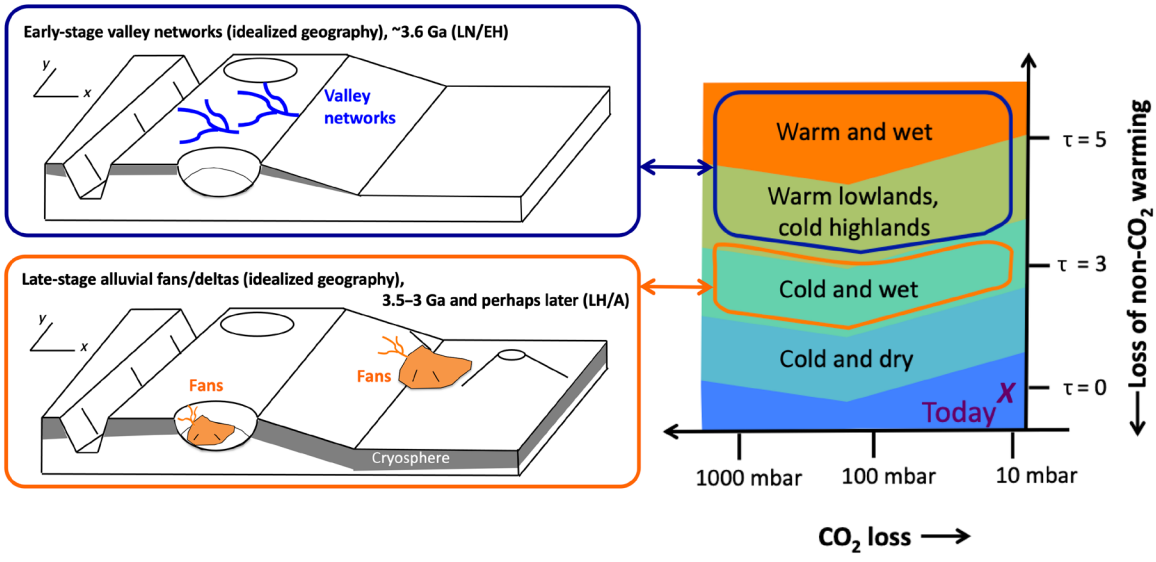

Fig. 6. Graphical summary of this study. (**Left column**) Simple (geographically idealized) schematic of changes over time, interpreted by analysis of elevation decline (Figs. 1 and 2) in comparison to the ensemble of GCMs (Figs. 3 and 4). (**Right column**) Cartoon summary of Fig. 5 illustrating that, within the framework of our model, shifts can occur with or without changes in P_{CO_2}, but very probably require a decline in non-CO_2 radiative forcing.

H_2-CO_2 collision-induced absorption. Similarly, Perseverance analysis of the texture and origin of carbonates (*50*) might help constrain P_{CO_2}. Conversely, the global constraints on long-term evolution provided here offer long-term global context for inherently local (and likely stratigraphically restricted) sample acquisition by the Mars Sample Return program.

Mars is the only world whose surface is known to have become uninhabitable. This study quantitatively compared geologic data to a climate model over different eras within Mars's wet-to-dry transition. Future models of the evolution of <3-6 Ga river-forming climates should satisfy the geologic constraints on the shifting location of rivers (Fig. 2). We used a simplified meltwater model to perform the first (although not the only possible) analysis of the causes of this downshift in Martian habitability. Within our model framework, changes over time in the spatial pattern of paleo-rivers suggest a waning greenhouse effect. Comparison of a grid of GCM simulations combining gray gas and CO_2 radiative forcing shows little sensitivity of river-relevant output to P_{CO_2}, but strong sensitivity to the strength of the non-CO_2 greenhouse forcing. Our results raise the possibilities that Mars had a thin (≤150 mbar) atmosphere throughout the river-forming era, and that Mars became uninhabitable as the result of constant-pressure cooling. This study does not rule out the hypothesis (*6*–*7*) that the end of surface habitability on Mars was ultimately driven by atmospheric decay, but suggests that loss of non-CO_2 radiative forcing (not loss of CO_2) played a dominant role in the changing spatial distribution of water flow from 3.6 Ga to 3.0 Ga.

MATERIALS AND METHODS

Geologic data

We used an existing valley network database [from (*17*)], compiled using Thermal Emission Imaging System (THEMIS) data. Our new fans/deltas database (Fig. 1B) is described in (*18*). This database was compiled by systematically searching between 90°N and 90°S using globally available Context Camera (CTX) images for fan-shaped deposits and their associated catchment areas. Details of how both databases were filtered and corrected for detectability bias are given in the Supplementary Materials.

Description of GCM simulations

MarsWRF is a version of the PlanetWRF GCM, itself derived from the terrestrial mesoscale WRF model (*23*–*24*). Model resolution is 5.0° × 3.75° (64 × 48 grid points) for longitude and latitude, respectively, with 40 model layers in height, spanning the surface to ~80 km. This resolution is typical for Mars GCMs. Further details are provided in the Supplementary Materials. For the gray gas, we use zero absorption coefficient for wavelengths less than 4.5 μm and an adjustable, constant absorption coefficient for wavelengths above 4.5 μm. The coefficient κ (m^2/kg) is chosen to produce a specified additional (non-CO_2) infrared optical depth, τ, at reference elevation (0 m). GCMs are run until the annual cycle has converged (typically <10 simulated years) at fixed orbital conditions. To get from the GCM model output to predicted meltwater runoff locations, we used a simplified meltwater model. The model assigns snow/ice to pixels that are calculated to have relatively low sublimation rate. Then, the model outputs a melt prediction for pixels where the temperature is warm enough for runoff. Further details, including how the predictions from the different GCMs were scored in comparison to the data, are given in the Supplementary Materials.

SUPPLEMENTARY MATERIALS

Supplementary material for this article is available at https://science.org/doi/10.1126/sciadv.abo5894

REFERENCES AND NOTES

1. J. P. Grotzinger, D. Y. Sumner, L. C. Kah, K. Stack, S. Gupta, L. Edgar, D. Rubin, K. Lewis, J. Schieber, N. Mangold, R. Milliken, P. G. Conrad, D. DesMarais, J. Farmer, K. Siebach, F. Calef III, J. Hurowitz, S. M. McLennan, D. Ming, D. Vaniman, J. Crisp, A. Vasavada, K. S. Edgett, M. Malin, D. Blake, R. Gellert, P. Mahaffy, R. C. Wiens, S. Maurice, J. A. Grant, S. Wilson, R. C. Anderson, L. Beegle, R. Arvidson, B. Hallet, R. S. Sletten, M. Rice, J. Bell III, J. Griffes, B. Ehlmann, R. B. Anderson, T. F. Bristow, W. E. Dietrich, G. Dromart,

J. Eigenbrode, A. Fraeman, C. Hardgrove, K. Herkenhoff, L. Jandura, G. Kocurek, S. Lee, L. A. Leshin, R. Leveille, D. Limonadi, J. Maki, S. McCloskey, M. Meyer, M. Minitti, H. Newsom, D. Oehler, A. Okon, M. Palucis, T. Parker, S. Rowland, M. Schmidt, S. Squyres, A. Steele, E. Stolper, R. Summons, A. Treiman, R. Williams, A. Yingst; MSL Science Team, A habitable fluvio-lacustrine environment at Yellowknife Bay, Gale crater, Mars. *Science* **343**, 1242777 (2014).
2. R. P. Irwin, K. W. Lewis, A. D. Howard, J. A. Grant, Paleohydrology of Eberswalde crater, Mars. *Geomorphology* **240**, 83–101 (2015).
3. J. A. Grant, S. A. Wilson, Late alluvial fan formation in southern Margaritifer Terra, Mars. *Geophys. Res. Lett.* **38**, L08201 (2011).
4. E. S. Kite, Geologic constraints on Early Mars climate. *Space Sci. Rev.* **215**, 10 (2019).
5. A. P. Ingersoll, Mars: Occurrence of liquid water. *Science* **168**, 972–973 (1970).
6. B. M. Jakosky, D. Brain, M. Chaffin, S. Curry, J. Deighan, J. Grebowsky, J. Halekas, F. Leblanc, R. Lillis, J. G. Luhmann, L. Andersson, N. Andre, D. Andrews, D. Baird, D. Baker, J. Bell, M. Benna, D. Bhattacharyya, S. Bougher, C. Bowers, P. Chamberlin, J. Y. Chaufray, J. Clarke, G. Collinson, M. Combi, J. Connerney, K. Connour, J. Correira, K. Crabb, F. Crary, T. Cravens, M. Crismani, G. Delory, R. Dewey, G. DiBraccio, C. Dong, Y. Dong, P. Dunn, H. Egan, M. Elrod, S. England, F. Eparvier, R. Ergun, A. Eriksson, T. Esman, J. Espley, S. Evans, K. Fallows, X. Fang, M. Fillingim, C. Flynn, A. Fogle, C. Fowler, J. Fox, M. Fujimoto, P. Garnier, Z. Girazian, H. Groeller, J. Gruesbeck, O. Hamil, K. G. Hanley, T. Hara, Y. Harada, J. Hermann, M. Holmberg, G. Holsclaw, S. Houston, S. Inui, S. Jain, R. Jolitz, A. Kotova, T. Kuroda, D. Larson, Y. Lee, C. Lee, F. Lefevre, C. Lentz, D. Lo, R. Lugo, Y. J. Ma, P. Mahaffy, M. L. Marquette, Y. Matsumoto, M. Mayyasi, C. Mazelle, W. McClintock, J. McFadden, A. Medvedev, M. Mendillo, K. Meziane, Z. Milby, D. Mitchell, R. Modolo, F. Montmessin, A. Nagy, H. Nakagawa, C. Narvaez, K. Olsen, D. Pawlowski, W. Peterson, A. Rahmati, K. Roeten, N. Romanelli, S. Ruhunusiri, C. Russell, S. Sakai, N. Schneider, K. Seki, R. Sharrar, S. Shaver, D. E. Siskind, M. Slipski, Y. Soobiah, M. Steckiewicz, M. H. Stevens, I. Stewart, A. Stiepen, S. Stone, V. Tenishev, N. Terada, K. Terada, E. Thiemann, R. Tolson, G. Toth, J. Trovato, M. Vogt, T. Weber, P. Withers, S. Xu, R. Yelle, E. Yiğit, R. Zurek, Loss of the Martian atmosphere to space: Present-day loss rates determined from MAVEN observations and integrated loss through time. *Icarus* **315**, 146–157 (2018).
7. R. M. Haberle, D. C. Catling, M. H. Carr, K. J. Zahnle, The Early Mars Climate System, in *The Atmosphere and Climate of Mars*, R. M. Haberle, R. T. Clancy, F. Forget, M. D. Smith, R. W. Zurek, Eds. (Cambridge Univ. Press, 2017), pp. 497–525.
8. D. C. Catling, J. F. Kasting, *Atmospheric Evolution on Inhabited and Lifeless Worlds* (Cambridge Univ. Press, 2017).
9. R. Wordsworth, F. Forget, E. Millour, J. W. Head, J.-B. Madeleine, B. Charnay, Global modelling of the early martian climate under a denser CO_2 atmosphere: Water cycle and ice evolution. *Icarus* **222**, 1–19 (2013).
10. C. I. Fassett, J. W. Head, The timing of martian valley network activity: Constraints from buffered crater counting. *Icarus* **195**, 61–89 (2008).
11. E. S. Kite, J. Sneed, D. P. Mayer, S. A. Wilson, Persistent or repeated surface habitability on Mars during the late Hesperian–Amazonian. *Geophys. Res. Lett.* **44**, 3991–3999 (2017).
12. P. B. Buhler, Timescales of fluvial activity and intermittency in Milna Crater, Mars. *Icarus* **241**, 130–147 (2014).
13. M. G. A. Lapôtre, A. Ielpi, The pace of fluvial meanders on Mars and implications for the western delta deposits of Jezero crater. *AGU Adv.* **1**, e2019AV000141 (2020).
14. R. E. Milliken, R. C. Ewing, W. W. Fischer, J. Hurowitz, Wind-blown sandstones cemented by sulfate and clay minerals in Gale Crater, Mars. *Geophys. Res. Lett.* **41**, 1149–1154 (2014).
15. W. Rapin, G. Dromart, D. Rubin, L. Le Deit, N. Mangold, L. A. Edgar, O. Gasnault, K. Herkenhoff, S. Le Mouélic, R. B. Anderson, S. Maurice, V. Fox, B. L. Ehlmann, J. L. Dickson, R. C. Wiens, Alternating wet and dry depositional environments recorded in the stratigraphy of Mount Sharp at Gale crater, Mars. *Geology* **49**, 842–846 (2021).
16. R. A. Craddock, T. A. Maxwell, Geomorphic evolution of the Martian highlands through ancient fluvial processes. *J. Geophys. Res. Planets* **98**, 3453–3468 (1993).
17. B. M. Hynek, M. Beach, M. R. T. Hoke, Updated global map of Martian valley networks and implications for climate and hydrologic processes. *J. Geophys. Res. Planets* **115**, E09008 (2010).
18. S. A. Wilson, A. M. Morgan, A. D. Howard, J. A. Grant, The global distribution of craters with alluvial fans and deltas on Mars. *Geophys. Res. Lett.* **48**, e2020GL091653 (2021).
19. M. Turbet, F. Forget, 3-D Global modelling of the early martian climate under a dense CO_2+H_2 atmosphere and for a wide range of surface water inventories. arXiv:2103.10301 [astro-ph.EP] (18 March 2021).
20. S. Bouley, D. Baratoux, I. Matsuyama, F. Forget, A. Séjourné, M. Turbet, F. Costard, Late Tharsis formation and implications for early Mars. *Nature* **531**, 344–347 (2016).
21. K. E. Scanlon, J. W. Head, J. L. Fastook, R. D. Wordsworth, The Dorsa Argentea formation and the Noachian-Hesperian climate transition. *Icarus* **299**, 339–363 (2018).
22. N. R. Alsaeed, B. M. Jakosky, Mars water and D/H evolution from 3.3 Ga to present. *J. Geophys. Res. Planets* **124**, 3344–3353 (2019).
23. M. I. Richardson, A. D. Toigo, C. E. Newman, PlanetWRF: A general purpose, local to global numerical model for planetary atmospheric and climate dynamics. *J. Geophys. Res.* **112**, E09001 (2007).
24. A. D. Toigo, C. Lee, C. E. Newman, M. I. Richardson, The impact of resolution on the dynamics of the Martian global atmosphere: Varying resolution studies with the MarsWRF GCM. *Icarus* **221**, 276–288 (2012).
25. R. D. Wordsworth, L. Kerber, R. T. Pierrehumbert, F. Forget, J. W. Head, Comparison of "warm and wet" and "cold and icy" scenarios for early Mars in a 3-D climate model. *J. Geophys. Res. Planets* **120**, 1201–1219 (2015).
26. A. M. Palumbo, J. W. Head, Early Mars climate history: Characterizing a "warm and wet" martian climate with a 3-D global climate model and testing geological predictions. *Geophys. Res. Lett.* **45**, 10249–10258 (2018).
27. J. N. Bahcall, M. H. Pinsonneault, S. Basu, Solar models: Current epoch and time dependences, neutrinos, and helioseismological properties. *Astrophys. J.* **555**, 990–1012 (2001).
28. C. I. Fassett, J. L. Dickson, J. W. Head, J. S. Levy, D. R. Marchant, Supraglacial and proglacial valleys on Amazonian Mars. *Icarus* **208**, 86–100 (2010).
29. E. S. Kite, I. Halevy, M. A. Kahre, M. J. Wolff, M. Manga, Seasonal melting and the formation of sedimentary rocks on Mars, with predictions for the Gale Crater mound. *Icarus* **223**, 181–210 (2013).
30. G. D. Clow, Generation of liquid water on Mars through the melting of a dusty snowpack. *Icarus* **72**, 95–127 (1987).
31. R. A. Wharton Jr., C. P. McKay, G. D. Clow, D. T. Andersen, G. M. Simmons Jr., F. G. Love, Changes in ice cover thickness and lake level of Lake Hoare, Antarctica: Implications for local climatic change. *J. Geophys. Res. Oceans* **97**, 3503–3513 (1992).
32. P. T. Doran, C. P. McKay, A. G. Fountain, T. Nylen, D. M. McKnight, C. Jaros, J. E. Barrett, Hydrologic response to extreme warm and cold summers in the McMurdo Dry Valleys, East Antarctica. *Antarct. Sci.* **20**, 499–509 (2008).
33. M. A. Mischna, V. Baker, R. Milliken, M. Richardson, C. Lee, Effects of obliquity and water vapor/trace gas greenhouses in the early Martian climate. *J. Geophys. Res. Planets* **118**, 560–576 (2013).
34. R. Ramirez, R. Craddock, The geological and climatological case for a warmer and wetter early Mars. *Nat. Geosci.* **11**, 230–237 (2018).
35. J. C. Andrews-Hanna, M. T. Zuber, R. E. Arvidson, S. M. Wiseman, Early Mars hydrology: Meridiani playa deposits and the sedimentary record of Arabia Terra. *J. Geophys. Res.* **115**, E06002 (2010).
36. S. D. Guzewich, M. J. Way, I. Aleinov, E. T. Wolf, A. Del Genio, R. Wordsworth, K. Tsigaridis, 3D simulations of the early martian hydrological cycle mediated by a H_2-CO_2 greenhouse. *J. Geophys. Res. Planets* **126**, (2021).
37. R. K. Kopparapu, R. Ramirez, J. F. Kasting, V. Eymet, T. D. Robinson, S. Mahadevan, R. C. Terrien, S. Domagal-Goldman, V. Meadows, R. Deshpande, Habitable zones around main-sequence stars: New estimates. *Astrophys. J.* **765**, 131 (2013).
38. M. Turbet, C. Boulet, T. Karman, Measurements and semi-empirical calculations of CO_2 + CH_4 and CO_2 + H_2 collision-induced absorption across a wide range of wavelengths and temperatures. Application for the prediction of early Mars surface temperature. *Icarus* **346**, 113762 (2020).
39. A. Palumbo, J. W. Head, Groundwater release on early Mars: Utilizing models and proposed evidence for groundwater release to estimate the required climate and subsurface water budget. *Geophys. Res. Lett.* **47**, e87230 (2020).
40. A. R. Khuller, P. R. Christensen, S. G. Warren, Spectral albedo of dusty martian H_2O snow and ice. *J. Geophys. Res. Planets* **126**, e2021JE006910 (2021).
41. P. R. Mahaffy, C. R. Webster, J. C. Stern, A. E. Brunner, S. K. Atreya, P. G. Conrad, S. Domagal-Goldman, J. L. Eigenbrode, G. J. Flesch, L. E. Christensen, H. B. Franz, C. Freissinet, D. P. Glavin, J. P. Grotzinger, J. H. Jones, L. A. Leshin, C. Malespin, A. C. McAdam, D. W. Ming, R. Navarro-Gonzalez, P. B. Niles, T. Owen, A. A. Pavlov, A. Steele, M. G. Trainer, K. H. Williford, J. J. Wray; MSL Science Team, The imprint of atmospheric evolution in the D/H of Hesperian clay minerals on Mars. *Science* **347**, 412–414 (2015).
42. S. J. Holo, E. S. Kite, S. A. Wilson, A. M. Morgan, The timing of alluvial fan formation on Mars. *Planet. Sci. J.* **2**, 210 (2021).
43. D. Y. Lo, R. V. Yelle, R. J. Lillis, J. I. Deighan, Carbon photochemical escape rates from the modern Mars atmosphere. *Icarus* **360**, 114371 (2021).
44. C. R. Webster, P. R. Mahaffy, G. J. Flesch, P. B. Niles, J. H. Jones, L. A. Leshin, S. K. Atreya, J. C. Stern, L. E. Christensen, T. Owen, H. Franz, R. O. Pepin, A. Steele; MSL Science Team, Isotope ratios of H, C, and O in CO_2 and H_2O of the Martian atmosphere. *Science* **341**, 260–263 (2013).
45. T. Owen, A. Bar-Nun, Comets, impacts, and atmospheres. *Icarus* **116**, 215–226 (1995).
46. R. M. Ramirez, R. Kopparapu, M. E. Zugger, T. D. Robinson, R. Freedman, J. F. Kasting, Warming early Mars with CO_2 and H_2. *Nat. Geosci.* **7**, 59–63 (2014).
47. R. Wordsworth, Y. Kalugina, S. Lokshtanov, A. Vigasin, B. Ehlmann, J. Head, C. Sanders, H. Wang, Transient reducing greenhouse warming on early Mars. *Geophys. Res. Lett.* **44**, 665–671 (2017).

48. R. A. Urata, O. B. Toon, Simulations of the Martian hydrologic cycle with a general circulation model: Implications for the ancient Martian climate. *Icarus* **226**, 229–250 (2013).
49. E. S. Kite, L. J. Steele, M. A. Mischna, M. I. Richardson, Warm early Mars surface enabled by high-altitude water ice clouds. *Proc. Natl. Acad. Sci. U.S.A.* **118**, e2101959118 (2021).
50. B. H. N. Horgan, R. B. Anderson, G. Dromart, E. S. Amador, M. S. Rice, The mineral diversity of Jezero crater: Evidence for possible lacustrine carbonates on Mars. *Icarus* **339**, 113526 (2020).
51. B. L. Ehlmann, C. S. Edwards, Mineralogy of the Martian surface. *Annu. Rev. Earth Planet. Sci.* **42**, 291–315 (2014).
52. M. P. Lamb, A. D. Howard, J. Johnson, K. X. Whipple, W. E. Dietrich, J. T. Perron, Can springs cut canyons into rock? *J. Geophys. Res.* **111**, E07002 (2006).
53. E. R. Kraal, M. van Dijk, G. Postma, M. G. Kleinhans, Martian stepped-delta formation by rapid water release. *Nature* **451**, 973–976 (2008).
54. M. G. A. Lapôtre, M. P. Lamb, Substrate controls on valley formation by groundwater on Earth and Mars. *Geology* **46**, 531–534 (2018).
55. E. Hauber, T. Platz, D. Reiss, L. le Deit, M. G. Kleinhans, W. A. Marra, T. de Haas, P. Carbonneau, Asynchronous formation of Hesperian and Amazonian-aged deltas on Mars and implications for climate. *J. Geophys. Res.* **118**, 1529–1544 (2013).
56. M. Turbet, C. Gillmann, F. Forget, B. Baudin, A. Palumbo, J. Head, O. Karatekin, The environmental effects of very large bolide impacts on early Mars explored with a hierarchy of numerical models. *Icarus* **335**, 113419 (2020).
57. R. M. Haberle, K. Zahnle, N. G. Barlow, K. E. Steakley, Impact degassing of H_2 on Early Mars and its effect on the climate system. *Geophys. Res. Lett.* **46**, 13355–13362 (2019).
58. K. Goddard, N. H. Warner, S. Gupta, J.-R. Kim, Mechanisms and timescales of fluvial activity at Mojave and other young Martian craters. *J. Geophys. Res. Planets* **119**, 604–634 (2014).
59. D. K. Weiss, J. W. Head, Extensive Amazonian-aged fluvial channels on Mars: Evaluating the role of Lyot crater in their formation. *Geophys. Res. Lett.* **44**, 5336–5344 (2017).
60. C. M. Dundas, A. S. McEwen, S. Diniega, C. J. Hansen, S. Byrne, J. N. McElwaine, The formation of gullies on Mars today, in *Martian Gullies and Their Earth Analogues*, S. J. Conway, J. L. Carrivick, P. A. Carling, T. De Haas, T. N. Harrison, Eds. (Geological Society, 2017), pp. 67–94, vol. 467.
61. S. W. Squyres, J. F. Kasting, Early Mars: How warm and how wet? *Science* **265**, 744–749 (1994).
62. E. S. Kite, D. P. Mayer, S. Wilson, J. Davis, A. S. Lucas, G. Stucky de Quay, Persistence of intense, climate-driven runoff late in Mars history. *Sci. Adv.* **5**, eaav7710 (2019).
63. T. A. Goudge, C. I. Fassett, J. W. Head, J. F. Mustard, K. L. Aureli, Insights into surface runoff on early Mars from paleolake basin morphology and stratigraphy. *Geology* **44**, 419–422 (2016).
64. J. M. Moore, A. D. Howard, Large alluvial fans on Mars. *J. Geophys. Res. Planets* **110**, E04005 (2005).
65. M. Mangold, G. Dromart, V. Ansan, F. Salese, M. G. Kleinhans, M. Massé, C. Quantin, K. M. Stack, Fluvial regimes, morphometry, and age of Jezero crater paleolake inlet valleys and their exobiological significance for the 2020 Rover Mission Landing Site. *Astrobiology* **20**, 994–1013 (2020).
66. G. G. Michael, Planetary surface dating from crater size-frequency distribution measurements: Multiple resurfacing episodes and differential isochron fitting. *Icarus* **226**, 885–890 (2013).
67. W. Luo, X. Cang, A. D. Howard, New Martian valley network volume estimate consistent with ancient ocean and warm and wet climate. *Nat. Commun.* **8**, 15766 (2017).
68. E. R. Kraal, E. Asphaug, J. M. Moore, A. Howard, A. Bredt, Catalogue of large alluvial fans in Martian impact craters. *Icarus* **194**, 101–110 (2008).
69. K. L. Tanaka, J. A. Skinner Jr., J. M. Dohm, R. P. Irwin III, E. J. Kolb, C. M. Fortezzo, T. Platz, G. G. Michael, T. M. Hare, Geologic map of Mars: USGS Scientific Investigations Map 3292 (2014).
70. F. Nimmo, K. Tanaka, Early crustal evolution of Mars. *Annu. Rev. Earth Planet. Sci.* **33**, 133–161 (2005).
71. D. E. Smith, M. T. Zuber, H. V. Frey, J. B. Garvin, J. W. Head, D. O. Muhleman, G. H. Pettengill, R. J. Phillips, S. C. Solomon, H. J. Zwally, W. B. Banerdt, T. C. Duxbury, M. P. Golombek, F. G. Lemoine, G. A. Neumann, D. D. Rowlands, O. Aharonson, P. G. Ford, A. B. Ivanov, C. L. Johnson, P. J. Mc Govern, J. B. Abshire, R. S. Afzal, X. Sun, Mars orbiter laser altimeter: Experiment summary after the first year of global mapping of Mars. *J. Geophys. Res.* **106**, 23689–23722 (2001).
72. T. A. Goudge, C. I. Fassett, J. W. Head, J. F. Mustard, K. L. Aureli, Extensive Noachian fluvial systems in Arabia Terra: Implications for early Martian climate. *Geology* **44**, 847–850 (2016).
73. M. A. Kreslavsky, J. W. Head, Mars climate history: Insights from impact crater wall slope statistics. *Geophys. Res. Lett.* **45**, 1751–1758 (2018).
74. R. M. E. Williams, R. J. Phillips, Morphometric measurements of martian valley networks from Mars Orbiter Laser Altimeter (MOLA) data. *J. Geophys. Res.* **106**, 23737–23751 (2001).
75. R. E. Grimm, S. C. Solomon, Tectonic tests of proposed polar wander paths for Mars and the Moon. *Icarus* **65**, 110–121 (1986).
76. R. I. Citron, M. Manga, D. J. Hemingway, Timing of oceans on Mars from shoreline deformation. *Nature* **555**, 643–646 (2018).
77. M. C. Malin, K. S. Edgett, B. A. Cantor, M. A. Caplinger, G. E. Danielson, E. H. Jensen, M. A. Ravine, J. L. Sandoval, K. D. Supulver, An overview of the 1985–2006 Mars Orbiter Camera science investigation. *Int. J. Mars Sci. Explor.* **4**, 1–60 (2010).
78. R. Beyer, K. Stack, J. L. Griffes, R. E. Milliken, K. E. Herkenhoff, S. Byrne, J. W. Holt, J. P. Grotzinger, An atlas of Mars sedimentary rocks as seen by HiRISE, in *Sedimentary Geology of Mars*, J. P. Grotzinger, R. E. Milliken, Eds. (SEPM Special Publication No. 102, 2012).
79. M. A. Mischna, C. Lee, M. Richardson, Development of a fast, accurate radiative transfer model for the Martian atmosphere, past and present. *J. Geophys. Res.* **117**, E10009 (2012).
80. R. M. Ramirez, J. F. Kasting, Could cirrus clouds have warmed early Mars? *Icarus* **281**, 248–261 (2017).
81. C. M. Dundas, S. Byrne, Modeling sublimation of ice exposed by new impacts in the martian mid-latitudes. *Icarus* **206**, 716–728 (2010).
82. W. J. Youden, Index for rating diagnostic tests. *Cancer* **3**, 32–35 (1950).

Acknowledgments: We thank B. Hynek, D. P. Mayer, A. O. Warren, N. Dauphas, J. Dickson, G. Stucky de Quay, R. Ramirez, D. Jablonski, HiWish, and the University of Chicago Research Computing Center (RCC). We thank five anonymous reviewers for timely, accurate, and useful comments. **Funding:** This work was supported by NASA (80NSSC20K0144 + 80NSSC18K1476). A portion of this work was performed at the Jet Propulsion Laboratory, California Institute of Technology, under contract with NASA. Resources supporting this work were provided by the NASA High-End Computing (HEC) Program through the NASA Advanced Supercomputing (NAS) Division at Ames Research Center. **Author contributions:** E.S.K. conceived the work, analyzed the data, carried out the GCM runs, and wrote the manuscript. M.A.M. and B.F. contributed to project design, GCM modeling, and interpretation. A.M.M. and S.A.W. carried out the survey of alluvial fans/deltas. M.I.R. supported the GCM modeling. **Competing interests:** The authors declare that they have no competing interests. **Data and materials availability:** All data needed to evaluate the conclusions in the paper are present in the paper and/or the Supplementary Materials. Additional data are stored at Zenodo (doi:10.5281/zenodo.6380945). The MarsWRF source code can be made available by Aeolis Research pending scientific review and a completed Rules of the Road agreement. Requests for the MarsWRF source code should be submitted to: M.I.R. (mir@aeolisresearch.com).

Submitted 14 February 2022
Accepted 31 March 2022
Published 25 May 2022
10.1126/sciadv.abo5894

ScienceAdvances

Changing spatial distribution of water flow charts major change in Mars's greenhouse effect

Edwin S. KiteMichael A. MischnaBowen FanAlexander M. MorganSharon A. WilsonMark I. Richardson

Sci. Adv., 8 (21), eabo5894. • DOI: 10.1126/sciadv.abo5894

Science Advances (ISSN) is published by the American Association for the Advancement of Science. 1200 New York Avenue NW, Washington, DC 20005. The title *Science Advances* is a registered trademark of AAAS.